Archive of Applied Mechanics
https://doi.org/10.1007/s00419-024-02589-3

ORIGINAL

Alexandros Tragoudas · Marta Alloisio · Elsayed S. Elsayed · T. Christian Gasser · Fadi Aldakheel

An enhanced deep learning approach for vascular wall fracture analysis

Received: 30 November 2023 / Accepted: 15 March 2024

Abstract This work outlines an efficient deep learning approach for analyzing vascular wall fractures using experimental data with openly accessible source codes (https://doi.org/10.25835/weuhha72) for reproduction. Vascular disease remains the primary cause of death globally to this day. Tissue damage in these vascular disorders is closely tied to how the diseases develop, which requires careful study. Therefore, the scientific community has dedicated significant efforts to capture the properties of vessel wall fractures. The symmetry-constrained compact tension (symconCT) test combined with digital image correlation (DIC) enabled the study of tissue fracture in various aorta specimens under different conditions. Main purpose of the experiments was to investigate the displacement and strain field ahead of the crack tip. These experimental data were to support the development and verification of computational models. The FEM model used the DIC information for the material parameters identification. Traditionally, the analysis of fracture processes in biological tissues involves extensive computational and experimental efforts due to the complex nature of tissue behavior under stress. These high costs have posed significant challenges, demanding efficient solutions to accelerate research progress and reduce embedded costs. Deep learning techniques have shown promise in overcoming these challenges by learning to indicate patterns and relationships between the input and label data. In this study, we integrate deep learning methodologies with the attention residual U-Net architecture to predict fracture responses in porcine aorta specimens, enhanced with a Monte Carlo dropout technique. By training the network on a sufficient amount of data, the model learns to capture the features influencing fracture progression. These parameterized datasets consist of pictures describing the evolution of tissue fracture path along with the DIC measurements. The integration of deep learning should not only enhance the predictive accuracy, but also significantly reduce the computational and experimental burden, thereby enabling a more efficient analysis of fracture response.

Keywords Soft biological tissue · Experimental data · Vascular tissue · Fracture · Deep learning · Attention residual U-Net architecture · Open-access source codes and data

1 Introduction

Clinical observations have shown that tissue failure and damage are important aspects influencing the evolution of vascular diseases [1–4]. The unique characteristics of soft tissue, being both a composite material and a living organism, make age a crucial factor influencing results. Many experimental setups designed for

A. Tragoudas · E. S. Elsayed · F. Aldakheel (✉)
Institute of Mechanics and Computational Mechanics, Leibniz Universität Hannover, Appelstrasse 9a, 30167 Hannover, Germany
E-mail: fadi.aldakheel@ibnm.uni-hannover.de

M. Alloisio · T. Christian
Solid Mechanics, Department of Engineering Mechanics, KTH Royal Institute of Technology, Stockholm, Sweden

Published online: 15 April 2024

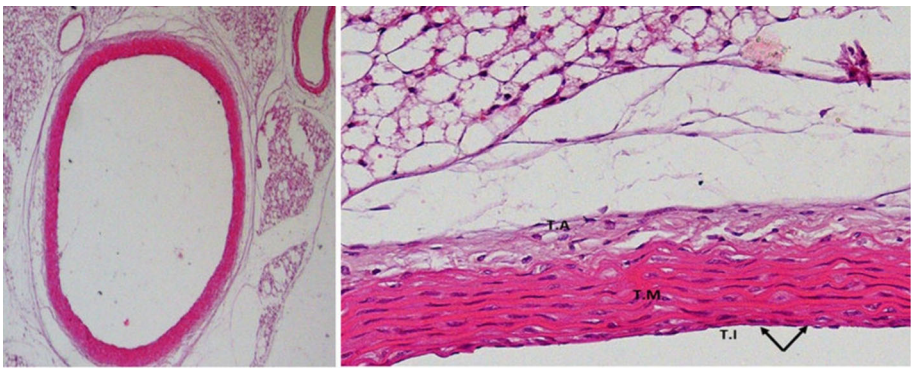

Fig. 1 Biological visualization of vascular tissue [11]

common materials often fall short in fully capturing the fracture properties of vessel walls. Most current experimental setups are designed to investigate common engineering materials, and as a result, they often fall short in fully capturing the fracture properties of vessel walls due to the unique characteristics of soft tissues. Numerous experimental findings have highlighted the important role of biochemomechanical factors [5–7], which contributes to the initiation and progression of vascular disorders. Despite various experimental setups having been utilized to collect data describing the mechanical properties of vascular tissue Fig. 1, crucial information required for the calibration and validation of materials models is often inadequately captured. This limitation arises from failures in accurately representing mechanical behavior, particularly during instances of failure and uncontrolled tissue fracture evolution [8]. As a result, these experimental data are incapable of providing a comprehensive understanding of vascular tissue failure.

Fundamentally all experimental setups face significant limitations to capture fully all mechanisms influencing the vascular tissue fracture. To surmount some of these challenges, the application of the symmetry-constrained compact tension (symconCT) test, coupled with digital image correlation (DIC), has been employed [9]. This approach enables the examination of tissue fracture in diverse porcine aorta specimens under varying conditions, aiming to capture and identify the material parameters influencing the propagation of soft tissue fracture. While these experiments, combined with digital image correlation (DIC) [10], allow for the observation of soft tissue fracture progression, the manual nature of this procedure requires significant physical effort. Consequently, recognizing potential challenges in physical interpretation, the adoption of deep learning to replace digital image correlation (DIC) data emerges as a promising avenue for the evaluation of the experimental data.

Over the past decades, there has been significant progress in numerical solutions, leading to increased accuracy in handling complex simulations, particularly in terms of both temporal and spatial aspects. These advancements had an impact to multiple fields, including a wide spectrum of applications, such as the simulation of cardiovascular disease evolution in coupled biochemomechanical material models [12–14], also in the investigation of material parameters describing the mechanical properties of a vascular tissue. Despite the continuing algorithmic progress [15], the implementation of parallelization architectures and the optimization of graphics processing units (GPUs) in the computation process, still in many cases the computational demand is high [16], especially in cases where the goal of assessing numerous material parameters is an essential part of the work.

In this study, a purely data-driven deep learning model is introduced as a computationally efficient solution method that is capable of providing a high level of accuracy. In comparison with the newly introduced approach of physics-based neural networks [17–21], an advantage of a data-driven model is that it does not require any preceding knowledge as for the science describing the problem [22]. In the last years, deep learning models have displayed an impressive ability to return substantial solid results in visual recognition tasks [23–26]. Yet, their success is limited when factors such as the size of the training datasets and network need to be taken under consideration [27]. These challenges show up in particular in the domain of biomedical image processing, where in most cases a huge amount of data translating into thousands of images is necessary to train a deep learning model [16]. In the presented contribution, the newly proposed architecture known as attention residual U-Net is implemented. The selection of this architecture is based on literature, which suggests that with a smaller dataset, this approach is expected to yield more accurate results compared to a traditional convolutional neural network (CNN) model [28–32]. The increased efficiency of the U-Net in segmentation

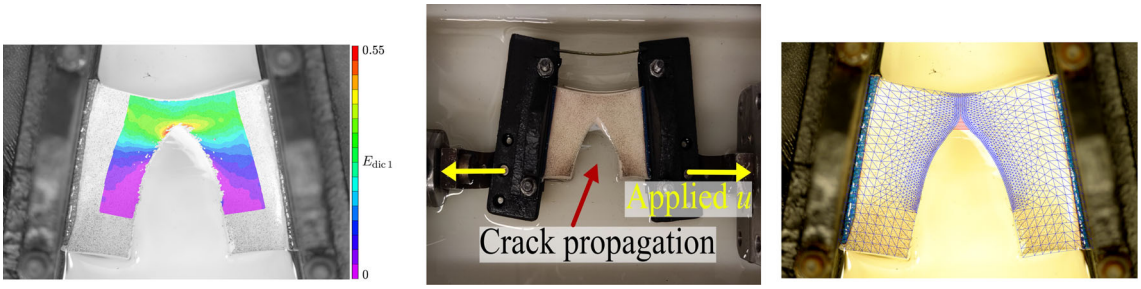

Fig. 2 Illustration of the symconCT fracture test of a porcine aortic specimen along with the DIC (left) and FEM mesh (right). Displacement u is applied to two clamps that are connected by an elastic beam. The design fosters stable and symmetrized fracture propagation, and the speckle pattern at the endothelial vessel wall surface supports DIC-based full-field strain measurements. The test is performed in physiological saline solution at 37 degrees Celsius

has been essential, since our input data come from physical experiments [9], which by their nature are limited and there is a lot of extra noise making it harder to identify the important features.

The structure of this work is as follows: In Sect. 2, a brief introduction to the symmetry-constrained compact tension (symconCT) experiment coupled with digital image correlation (DIC) along with the FEM model is presented. The architecture of our U-Net model will be shown in Sect. 3, while in Sect. 4 the numerical results are presented and discussed to explain the findings. Lastly, in Sect. 5, possibilities for extending this work are intended to be discussed. Open-access source codes and data (https://doi.org/10.25835/weuhha72) are provided, constituting a convenient platform for future developments.

2 Experimental–numerical approach studying fracture mechanisms

The symmetry-constrained compact tension (symconCT) fracture test enhances the classical CT test by inserting an elastic metal beam that connects two 3D printed clamps. Besides pre-straining the approximately 30x35 mm^2 tissue specimen, the beam forces the clamps to open symmetrically, see Fig. 2.

Prior to testing, a 10 mm pre-notch was excised in the central portion of the test specimen, resulting in a stress concentration at the tip. This concentration ensures that the fracture propagates from that point. Tensile loading, in either the axial or circumferential direction, was applied orthogonal to the pre-notch at 3 mm/min. The tensile machine (ADMET eXpert 4000 Universal Testing System, ADMET, Inc.) recorded the applied force and clamp displacement at 100 Hz, and a digital camera (Nikon D300S equipped with a lens Sigma 105 mm F2.8 DG DN MACRO, Sigma Corporation) took images at 1 Hz for digital image correlation (DIC) analysis (Vic2D, Correlated Solutions, Inc.).

The symconCT test allows for stable and controlled crack propagation and therefore enables full-field surface displacement measurements, in particular ahead of the crack tip. All details concerning the experimental setup are reported in [9].

2.1 Comparison of the experimental recording and FEM results

With the aim of identifying material parameters from the experimental recordings, 2D plane stress FEM models is employed in line with [33]. Those models represent the individual dimensions and fracture paths of selective specimens. A quasi-nonlinear viscoelastic model, employing the isotropic Yeoh strain energy density, is hereby utilized to describe the behavior of the aortic vessel wall tissue. Although this form of constitutive relation has been proposed for rubberlike materials [34], it has also been frequently employed to describe the mechanics of the aortic wall, especially for aneurysmatic tissue [35]. We assumed irreversible fracture-related processes to accumulate in a fracture process zone that develops ahead of the crack tip, an established approach in fracture modeling [36,37]. An isotropic cohesive zone was therefore employed. Next, we provide a summary of our FEM model.

2.1.1 Governing equations

We chose to employ a viscoelastic tissue description, given the high strain rates observed ahead of the crack tip in the symconCT test [9]. In this regard, the free energy function defining vascular tissue is formulated as follows

$$\psi = \psi^{\infty} - \sum_{k=1}^{p} g_k \left(1 - e^{-t/\tau_k}\right) \psi^{\infty} \quad \text{with} \quad \psi^{\infty} = c_1(I_1 - 3) + c_2(I_1 - 3)^2 \quad \text{and} \quad I_1 = \text{tr}\left[\boldsymbol{F}^T \boldsymbol{F}\right]. \quad (1)$$

The Prony series parameters g_k and τ_k are given in [33] and have been extracted from the literature [38]. The elastic properties ψ^{∞} of the media are captured by the isotropic Yeoh strain energy density. Hereby, the material parameters c_1 and c_2 are to be identified from the symconCT test recordings and $\boldsymbol{F}$ is the material deformation gradient tensor. For describing fracture behavior, we employed an isotropic cohesive zone model. The fracture energy (the energy to form the unit area of fracture surface in the reference configuration) then reads

$$G = \frac{1}{2}\left[K_0 \delta_0^2 + K_s(\delta_{\max} - \delta_0)^2\right], \quad (2)$$

with the elastic limit separation δ_0, the stiffness K_0 and the opening at complete fracture $\delta_{\max}$. The cohesive strength T_0 and the fracture energy G are parameters to identify from the symconCT test recordings, while K_0 was fixed to a value that displayed minimal elastic gap opening in preliminary numerical simulations. For the inverse parameters identification, the scalar objective function

$$\phi(\mathbf{p}) = \beta \phi_{\text{force}}(\mathbf{p}) + (1 - \beta)\phi_{\text{defo}}(\mathbf{p}), \quad (3)$$

is minimized, where $\mathbf{p} = (c_1, c_2)$ and $\beta = 0.5$ weights represent the normalized errors in clamp force ϕ_{force} and Green–Lagrange strains ϕ_{defo}, respectively. At this stage, the identification considered experimental recording prior to any visible signs of crack propagation. Green–Lagrange strains have been compared at colocated coordinates within a region of 10 x 5 mm^2 on the specimen surface. The comparison is made at clamp displacement increments of 1 mm, and further details are reported elsewhere [33]. Finally, at fixed c_1 and c_2 parameters, the minimization of $\phi_{\text{force}}(\mathbf{p})$, identified $\mathbf{p} = (T_0, G)$, where T_0 and G denote the cohesive strength and the fracture energy of vessel wall tissue, respectively. Further details are reported in our previous work [33].

3 Deep learning model implementation

In this work, we implemented an enhanced U-Net architecture known as attention residual U-Net [39,40]. The main idea behind the structure of a classical U-Net model as in [16] implies the improvement of a traditional contracting path with embedded successive layers. The denoting advantage of a U-Net architecture is the concatenation of features obtained during the downsampling in form of skip connections with the upsampling output. This method allows to store important information and hence create a more refined output in the deeper layers of the model. In most common U-Net models, the expanding path follows a configuration similar to the contracting path, resulting in the distinctive U-shaped form.

3.1 Network architecture

Our network architecture is illustrated in Fig. 3. It consists of a contracting path (left side), a bottleneck (central side) and an expanding path (right side) [16,41]. The arrows navigating from the contracting to the expanding path refer as skip connections. The purpose of the skip connections is to store extra information from important features, where the upsampling outputs are concatenated with skip connections to increase the localization of features, leading to an enhanced final prediction. In this work, a more sophisticated U-Net architecture is implemented using the attention and residual techniques [39,40]. The attention mechanism allows the network to emphasize in important features, enabling focused attention on critical regions. The integration of residual connections aids in reducing information loss during training, ensuring more efficient and stable learning. The model is further enhanced with the implementation of a Monte Carlo dropout technique [42,43]. This method

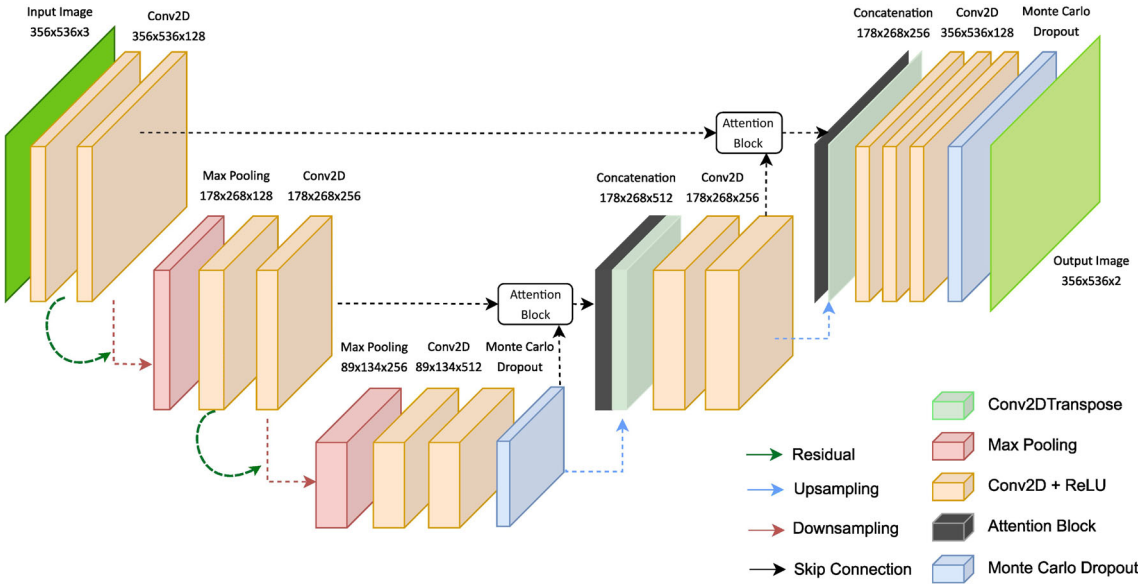

Fig. 3 Attention residual U-Net architecture, enhanced with a Monte Carlo dropout technique

acts like a Bayesian approach, working during both training and prediction. We chose it because our study involves a lot of nonlinearity, mainly due to the unique properties of soft tissue and the use of real experimental data as input. These real-world data often contain a high ratio of noise, making the training process more challenging. The architectural design of this model is structured around two downsample blocks, a bottleneck and two upsample blocks.

In each downsample block parts of the contracting path, the residual technique is implemented in order to increase the efficiency and hence reduce the loss of information. This implies that within each downsample block, its input tensor cuts across two paths. In the primary path, two 2D convolutions with a filter size 3 x 3 are applied, each succeeded by a rectified linear unit (ReLu) activation function. Simultaneously in the secondary path, this tensor undergoes through a single convolution, leading to the creation of shortcut path. These steps are followed by the addition of the outputs from both paths and a ReLu activation. The output tensor experiences a bifurcation; hence, it could be seen as the creation of two instances. The first instance contains the 2 x 2 max pooling operation with a stride of 2, where the output tensor of this operation will be the input information for the subsequent downsample block, while in the second instance this tensor will have a significant influence during the upsampling process.

It should be denoted that within each downsampling step, the number of filters is doubled. As expected, the tensor from the second instance influences the upsampling process within two different steps in the computation. Firstly it goes through a convolution and later enhances the upsampling process, while in another steps it contributes to final outcome with its original information, before the appliance of the convolution. This dual contribution leads to an increased capability of the model to identify and refine the important features of the investigated problem. This process repeats itself till the bottleneck is reached.

For the expanding path a similar approach takes places, but one significant difference is that additionally the mechanism of attention is implemented. The core advantage of the attention technique is that it allows to lay more focus into the critical region and capture the essential features. This requires two important components known as the gate block and attention block [39]. The gate blocks precede the attention block and store information, which will later be concatenated with the output from the attention block. In the attention block, processes such as convolution, activation, upsampling and concatenation with skip connections are applied.

On the output tensor of the last upsampling block, a final convolution and activation are applied, resulting in the desired output tensor of the deep learning model. This final output tensor translates to the predicted image. The integration of these enhancement techniques in both the contracting and expanding path leads to an increased accuracy of the model's predictions, through the reduction of loss information and better feature identification. Figure 3 displays an illustrative representation of our model to make it easier for the readers to understand its architecture.

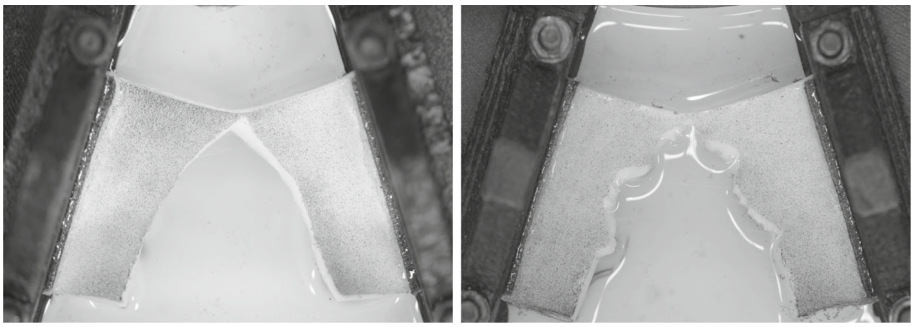

Fig. 4 Samples in grayscale, showing the vertical and circumferential crack

3.2 Training

The input data for our numerical model refer to grayscale images as shown in Fig. 4 with 3 channels, each image possessing dimensions of 536 x 356. These images show evolution of vascular tissue fracture at various time steps. While grayscale images are typically represented as single-channel images, a multi-channel representation of grayscale images is still possible for the representation of tissue fractures, a common approach in biomedical image processing [44].

On the other hand, the label data as shown in Fig. 5 have a physical interpretation representing the displacement distribution. The label data are array matrices, where their two channels denote the u and v displacements and hence accordingly the displacements in the X and Y directions. Each pixel of the label data holds a numerical displacement value. The label data are reconstructed from numerical information obtained through the DIC (digital image correlation) software, which is stored in .csv files. These files were used to generate the displacements distribution images. An important aspect is that the DIC outputs pixel coordinates are saved in these files with respect to the reference configuration along with their displacements u and v. To align our label data with the input data—given that our grayscale images describe the vascular tissue fracture in the current configuration—we implement a transformation of our labels between the configurations, see Eq. (4). This implies the transformation into the Eulerian configuration, ensuring a compatibility between the input and label data, leading to an increased effective model training.

$$x = X + u, \tag{4}$$

It is worth mentioning that during preprocessing, the dataset is shuffled. Normally, since the fracture exhibits a time dependency, a sequential approach should have been taken into account. However, the main goal of this work is not to forecast the evolution of the crack; hence, the time dependency does not have any influence on the predictions. Currently, the development of a new sequential model is in process, where the time dependency will be explicitly included.

In the context of deep learning models, the choice of the initial weights could have a significant influence to the convergence of the solution. A common approach used in many cases refers to the known "he-normal" approach for weight initialization of the convolution layers.

As known, the performance of a deep learning model depends strongly onto the various hyperparameters; therefore, a study case is conducted to identify their influence such as the number of filters and the starting point of the learning rate, with the outer goal to find the best combination of these hyperparameters, which it should translate to an increased final performance. The final outcomes revealed that initializing the learning rate at 1e-4 leads to better and faster model convergence. To improve the efficiency of the learning process, it is important to adjust the learning rate continuously. In this work, the Adam optimizer is utilized, which combines both momentum and RMSProp techniques. The parameters $\beta_1 = 0.9$ and $\beta_2 = 0.999$ control the exponential decay of the moments used in computing the averages of gradients. The parameter ϵ (holding the value of 10^{-7}) is only added in order to prevent division with respect to zero. Conversely it is observed that an increase in the number of filters did not have any significant positive influence. According to the literature, normalizing both the input and label data is often recommended to speed up the training process and improve results simultaneously. However, in this case we noticed the normalization of the output data had a negative effect. An assumption on our part is that the pixel values in our label data in this particular case have a physical interpretation, unlike other cases documented in the literature. Therefore, the normalization technique has been applied only to the input data as part of the preprocessing steps.

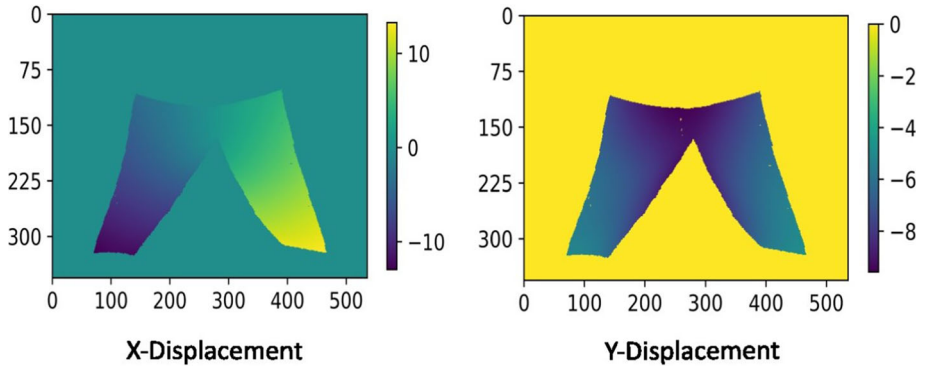

Fig. 5 Example of label data, showing the horizontal and vertical displacement distribution

In the presented contribution, the images are originally quite large and have been preprocessed to reduce their size. The large size of the images often causes GPU memory issues. To overcome this difficulty, a large batch size is typically chosen to reduce training time. However, to prevent memory issues, we consider a batch size of a single image. The training method is enhanced with advanced techniques like the reducing learning rate, early stopping and checkpoint. In the function for reducing learning rate, the evolution of the validation loss is monitored. In this work, the patience is chosen to be 100 epochs. If this limit is exceeded, the learning rate is reduced by a factor $= 0.1$ while a threshold of 0.0001 in the learning rate is considered to be a significant change. The early stopping technique monitors the validation loss, and if there is no significant change in its value after a patience of 200 epochs, the training process automatically stops. To ensure that the model with the lowest validation loss is captured, the checkpoint function stores the current weights of the most efficient model.

Such approaches ensure efficient model convergence while minimizing unnecessary computational costs. These techniques are meant to be activated, only if there is no improvement in the validation loss after a certain patience period. Particular strategies intent to increase overall the efficiency of the deep learning model.

4 Results and discussions

As mentioned in previous sections, our dataset is derived from experimental tests, particularly from the experimental setup introduced in [9], known as the symmetry-constrained compact tension (symconCT) experiment. This experimental design considers two loading cases. The first case involves external loading orthogonal to the fibers of the vascular tissue, resulting in a straight crack path. In the second case, circumferential loading causes the crack, leading to a zigzag fracture pattern, see Fig. 4. The focus of this work has been on the axial loading cases. The analysis of zigzag fracture pattern will be explored in future work.

For this study, 20 samples were provided, as shown in Fig. 6. Each sample represents an average of 500 images, illustrating the evolution of the fracture at various time steps. This resulted in a total dataset of approximately 10,000 images representing the displacement distribution of vascular tissue and the corresponding geometry as grayscale images. In this work, it is chosen to partition our data into three subsets referred as the training, validation and test datasets. The main goal is to train a model capable of replacing the DIC evaluation method by providing a faster yet sufficiently accurate solution, closely approximating the ground truth obtained through the DIC approach. To this end, the data are split into three sets with a percentage distribution of 90%, 5% and 5% for the training, validation and test datasets, respectively. This corresponds to approximately 8100, 450 and 450 images in each dataset. Two samples out of the 20 were kept intentionally out of the training process. This approach is taken in order to be able to evaluate the performance of the model on an entirely new and unseen geometries, therefore returning a first feedback, if the model shows the first glimpses for a possible generalization.

As mentioned, the ultimate goal ideally would be to create a model capable of delivering fast and highly accurate results for generalized cases. The initial step is to verify that the model can make accurate predictions for vascular tissue geometries, which were included in the training process. Figure 7 demonstrates the predictions of our most recent deep learning model for a seen geometry. The first row displays the input data, meaning the grayscale vascular tissue image at different time steps during the fracture. The second and third

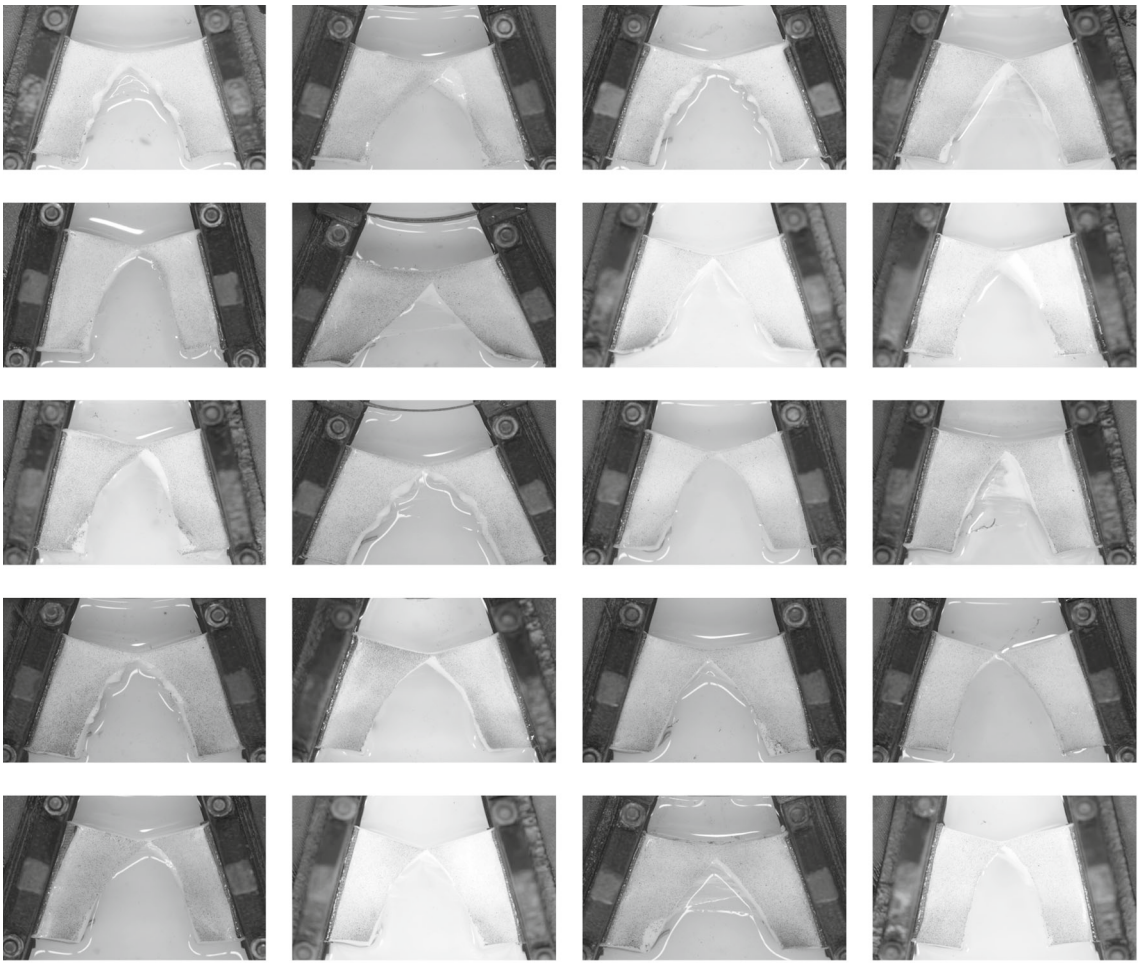

Fig. 6 Training, validation and test samples

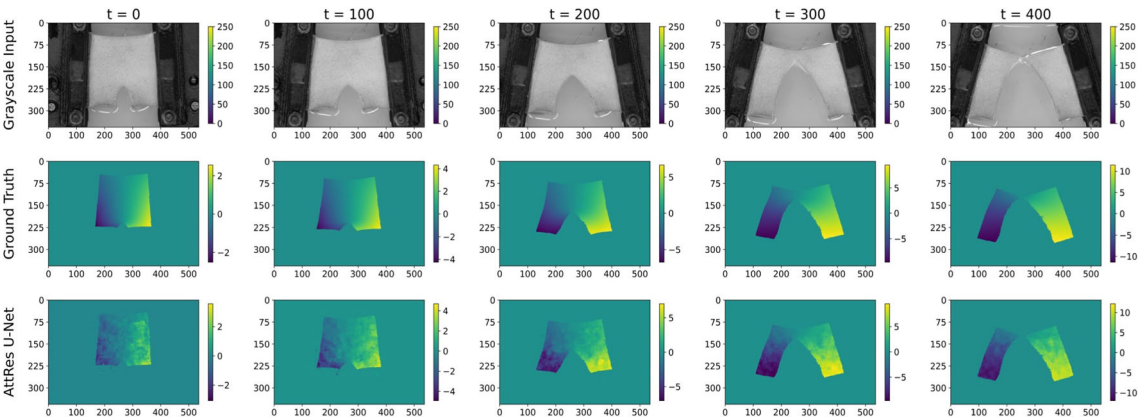

Fig. 7 Prediction fracture evolution of seen geometry: displacement distribution in X direction

Table 1 Performance comparison between seen and unseen geometry

Index of model	Technique	Amount of samples	Number of filters	Batch size
(i)	Classical U-Net	9	256	1
(ii)	Attention residual U-Net	9	256	1
(iii)	Attention residual U-Net	18	256	1
(iv)	Attention residual U-Net	9	256	8
(v)	Monte Carlo attention residual U-Net	9	256	8

rows show the displacement distribution for the X direction, depicting the ground truth and the prediction from the deep learning model, respectively. As evident from the figure, the model efficiently predicts both the geometry and numerical values of the displacement distribution, ensuring the potential to yield accurate results closely aligned with the ground truth.

An essential aspect of this contribution involves comparing prediction outcomes between a known geometry and a generalized one. This is illustrated in Fig. 8, where the displacement distribution in the y direction is visualized. A qualitative error measurement confirms that the model produces accurate predictions for both the tissue geometry during fracture and the numerical values of displacement in the y direction for the known (seen) geometry. However, when the model attempts to predict outcomes for a generalized case (unseen geometry), where no images of the tissue sample were included in the training process, it does not provide the ideal representation as in the seen case. Remarkably, the deep learning model was able to predict the crack surface for this generalized unseen case, demonstrating its potential for future development.

Additionally in Table 2, two quantitative error measurements are presented. The model performance is measured in a quantitative way by the mean absolute percentage error (MAPE) for both channels of the image and hence the predicted X- and Y-displacement distribution. The MAPE is defined as

$$\text{MAPE} = \frac{1}{n}\sum_{i=1}^{n}\left|\frac{y_i - \hat{y}_i}{y_i}\right| \qquad \text{and} \qquad R^2 = 1 - \frac{\sum_{i=1}^{n}(y_i - \hat{y}_i)^2}{\sum_{i=1}^{n}(y_i - \bar{y}_i)^2} \tag{5}$$

where $\hat{y}_i$ is the predicted value and y_i is the true value obtained by the DIC software. Another method to evaluate the performance of the model is the R^2-score as defined in Eq. (5), also known as the coefficient of determination, which is a statistical measure that shows how well the deep learning model approximates the actual data. R^2-score usually has a value in range between 0 and 1, defined as in terms of the mean value $\bar{y}_i$, where the values closer to 1 represent a model with better performance.

During this work, variations of U-Net architectures were adopted and a study case regarding the influence of hyperparameters is conducted. These models are presented in Table 1. The MAPE and R^2-score values for each channel of the displacement distribution are given in Table 2. for each deep learning model. As it was expected, the enhancement of the attention residual U-Net model (case 4) with the Monte Carlo technique (case 5) had an positive influence and all error measurements showed a reduction of the error. The same conclusion is also made by comparing the classical U-Net architecture (case 1) to the extended attention residual model (case 2). Furthermore, the increase in the batch size had also an impact in the reduction of the error as it shown in the difference between cases 2 and 3. For a seen geometry, all deep learning models return considering the R^2-score method less than 1% error. The best model manages to achieve less than 5% using the evaluation method of MAPE. An interesting observation is by examining the evaluation of an unseen geometry. It is to observe that all models, even though their accuracy is still not satisfying, manage easier to predict the displacement distribution in the Y direction than in the X direction.

While the results of the proposed model for generalized cases may not yet be ideal, it is important to consider the limitations of the data. In this work, actual experimental data are utilized rather than artificial ones tailored specifically for this study case. Despite this limitation, the model demonstrates promising predictions. This suggests the potential for achieving satisfactory results with further extensions and improvements. Such a development could lead to a significant reduction in evaluation effort.

4.1 Comments of the proposed deep learning model

In the initial stages of this work, following literature recommendations for biomedical image processing, we implemented a classical U-Net architecture. As suggested by [16], this method is considered the most

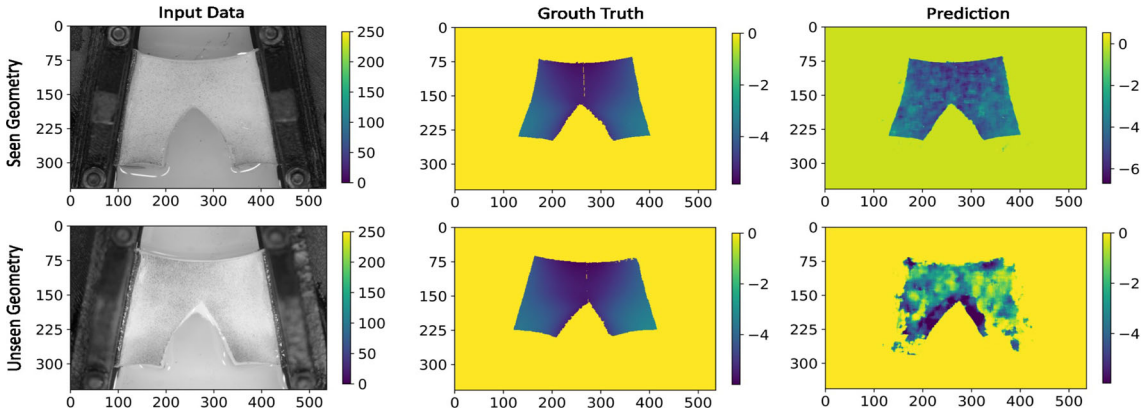

Fig. 8 Prediction quality comparison between seen and unseen geometry

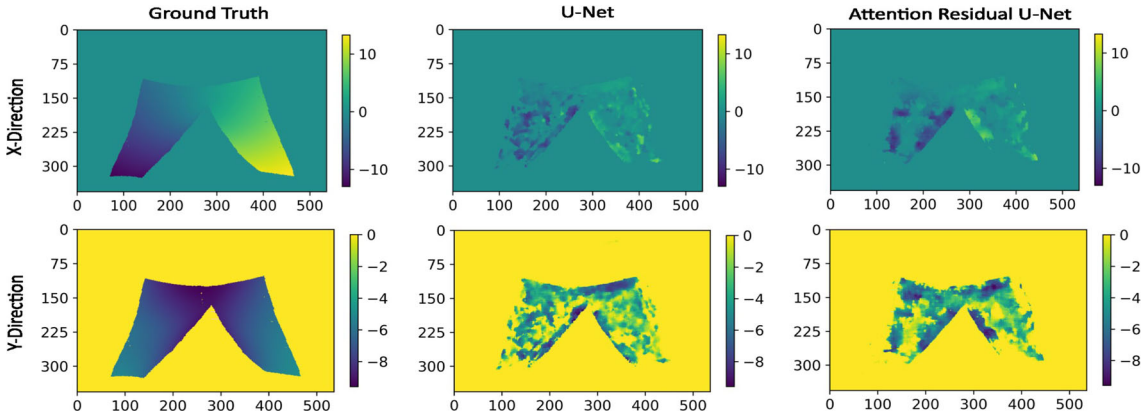

Fig. 9 Comparison between classical U-Net and enhanced attention residual U-Net architecture

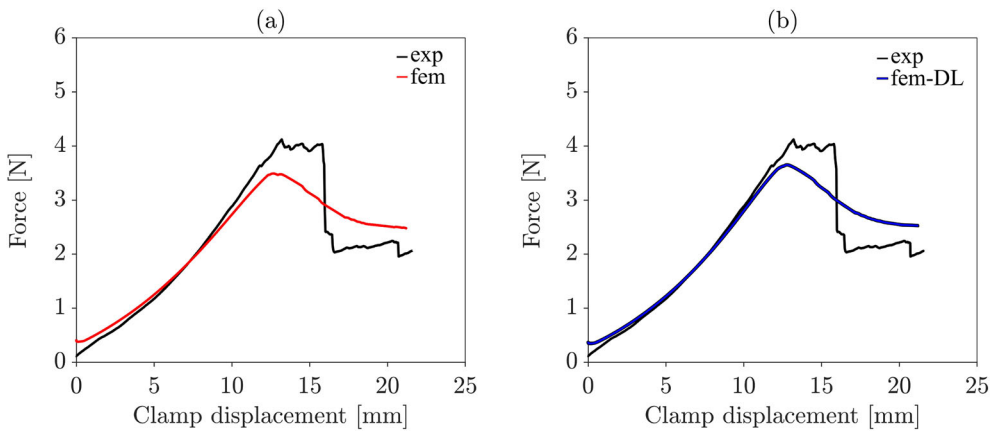

Fig. 10 Force versus clamp displacement recorded experimentally (black) and predicted by the calibrated FEM models (red). **a** FEM results with material parameters as identified from the experimentally recorded force–clamp displacement curve and the DIC measurements, see [33]. **b** FEM results with material parameters as identified from the experimentally recorded force–clamp displacement curve and the deep learning generated surface displacements. (Color figure online)

Table 2 Performance comparison: R^2-score and MSE measurements

Type of error	Index of model	X-disp	Y-disp
R^2-score	(i)	0.988	0.986
	(ii)	0.990	0.989
	(iii)	0.973	0.972
	(iv)	0.993	0.993
	(v)	0.998	0.995
MSE	(i)	2.3%	3%
	(ii)	3.2%	2.4%
	(iii)	5.2%	6.8%
	(iv)	1.2%	1.7%
	(v)	0.9%	1.3%

suitable for addressing such problems. As observed in the later section, the results for a generalized case were not ideal. Further exploration of the literature revealed that more sophisticated U-Net architectures could potentially enhance the model and yield the desired results. Consequently, attention [39] and residual [40] mechanisms were implemented to extend the classical U-Net architecture and increase the efficiency of the model. The residual technique leads to a reduction of the loss of important information during training, while the attention mechanism helps the deep learning model to lay more focus on critical regions. Figure 9 visualizes the influence of attention and residual mechanisms on the final predictions for both a known (seen) geometry and a generalized case. As expected, given that the classical U-Net model was already producing good results for known geometries, the incorporation of attention and residual techniques in this case did not yield noticeable differences. However, in generalized cases, the positive influence of attention and residual mechanisms becomes clear. Hereby, the model not only predicts the geometry of the vascular tissue more accurately but, more importantly, exhibits an increase in efficiency in predicting numerical values representing the displacement distribution.

4.2 Model validation

Another crucial aspect in validating the quality of this model involves utilizing the predicted data to assess the feasibility of substituting the DIC data with the model's current form.

Given purely experimentally recorded data, the parameter identification method described in Sect. 2.1 resulted in bulk material properties of $c_1 = 20.39$ kPa, $c_2 = 62.91$ kPa, and fracture properties of $T_0 = 260.60$ kPa, $G = 0.578$ kJ m^{-2}, in line with [33]. The FEM model reasonably recovered the experimentally recorded force–displacement curve, as illustrated by Fig. 10a.

In contrast, when utilizing the attention residual U-Net predicted displacement field alongside the experimentally recorded force–clamp displacement curve, the identification process resulted in $c_1 = 17.99$ kPa, $c_2 = 69.71$ kPa, as well as $T_0 = 366.75$ kPa, $G = 0.531$ kJ m^{-2}, respectively. The hybrid FEM-DL predicted force–clamp displacement curve again reasonably matched the experimental recordings, see Fig. 10b. The results obtained with this approach are notably more promising and superior when compared to those of a pure finite element method-based model in Fig. 10a. Hence, the proposed deep learning model generated displacements resulted in the identification of similar mechanical tissue properties, as in Fig. 10.

5 Conclusion

This work represented the initial step in constructing a deep learning model with the primary goal of leveraging and, consequently, reducing human and computational effort in the evaluation of experimental data.

In this paper, an attempt has been made to encompass a broader range of potential cases, aiming to gain a better understanding of the actual quality of results produced by the model. As demonstrated in Fig. 7, the attention residual model [16,39,40] successfully captures and recreates the intricate details of tissue geometry post-fracture for a known specimen included in the training dataset. Additionally, it accurately computes numerical values representing the displacement distributions. On the other hand, there is room for improvement when the model attempts to evaluate a generalized case, as illustrated in Fig. 9. Recognizing this limitation during the initial phase of development, various methods were explored to enhance its efficiency. One approach

involved implementing a more sophisticated U-Net architecture, incorporating the mechanisms of attention and residual. The results clearly demonstrate the expected positive influence of these mechanisms in the final results. The enhanced model exhibits a better approximation of the numerical values in the distribution and captures the tissue geometry more effectively. However, it remains evident that there is still room for improvement, as the quality of the generalized test cases should at least match the quality of the seen geometries. An important aspect that further motivates us to continue working in this direction stems from the practical implementation of the U-Net data in the inverse parameter identification. The initial partially positive outcomes obtained from the simulations, as illustrated in Fig. 10, emphasize the substantial impact that a refined model could have on the overall workflow process. This is especially noteworthy given that these kinds of approaches can be continuously extended.

In the short term, some key features to be included involve creating a generalized U-Net model capable of predicting both axial and circumferential cases. Additionally, there is consideration for implementing physics-based machine learning models [17–20,45–49], as this could enhance the efficiency of the model and yield more robust results, leveraging the knowledge of physics in the fracture process. Another approach involves extending the U-Net architecture to Up-Net. In theory, this extension could significantly improve the output, as the model would take into consideration a variety of physical quantities, as demonstrated in [50]. As expected there is still a long path for improvement in front of us, but since these first results show a first promise for lifting the effort away from repetitive tasks and in shifting our efforts in the correct direction, meaning the continual evolution in the research of the cardiovascular tissue disorders.

Acknowledgements Fadi Aldakheel gratefully acknowledges support for this research by the "German Research Foundation" (DFG) through the SFB/TRR-298-SIIRI—Project-ID 426335750.

Author contribution AT and ESE were involved in modeling, implementation and writing the first draft. MA and TCG were responsible for experimental data. FA contributed to modeling, implementation, writing and reviewing the paper, supervision and funding.

Funding Open Access funding enabled and organized by Projekt DEAL.

Data availability Open-access source codes and data, which can be used to reproduce all the examples, are now available online: https://doi.org/10.25835/weuhha72.

Declarations

Conflict of interest The authors declare no competing interests.

References

1. Golledge, J.: Abdominal aortic aneurysm: update on pathogenesis and medical treatments. Nat. Rev. Cardiol. **16**, 225–242 (2019)
2. Song, P., Fang, Z., Wang, H., Cai, Y., Rahimi, K., Zhu, Y., Fowkes, F.G.R., Fowkes, F.J., Rudan, I.: Global and regional prevalence, burden, and risk factors for carotid atherosclerosis: a systematic review, meta-analysis, and modelling study. Lancet Global Health **8**, e721–e729 (2020)
3. Libby, P., Buring, J. E., Badimon, L., Hansson, G. K., Deanfield, J., Bittencourt, M. S., Tokgozoglu, L., Lewis, E. F.: Atherosclerosis. Nat. Rev. Dis. Prim. **5** (2019). Cited by: 1340
4. Zohdi, T.: A computational framework for network modeling of fibrous biological tissue deformation and rupture. Comput. Methods Appl. Mech. Eng. **196**, 2972–2980 (2007)
5. Baeyens, N., Schwartz, M.A.: Biomechanics of vascular mechanosensation and remodeling. Mol. Biol. Cell **27**, 7–11 (2016)
6. Stone, P.H., Saito, S., Takahashi, S., Makita, Y., Nakamura, S., Kawasaki, T., Takahashi, A., Katsuki, T., Nakamura, S., Namiki, A., et al.: Prediction of progression of coronary artery disease and clinical outcomes using vascular profiling of endothelial shear stress and arterial plaque characteristics: the prediction study. Circulation **126**, 172–181 (2012)
7. Bäck, M., Gasser, T.C., Michel, J.-B., Caligiuri, G.: Biomechanical factors in the biology of aortic wall and aortic valve diseases. Cardiovasc. Res. **99**, 232–241 (2013)
8. Cowin, S.C., Humphrey, J.D.: Cardiovascular Soft Tissue Mechanics. Springer, Berlin (2001)

9. Alloisio, M., Chatziefraimidou, M., Roy, J., Gasser, T.C.: Fracture of the porcine aorta. Part 1: symconct fracture testing and DIC. Acta Biomater. **167**, 147–157 (2023)
10. McCormick, N., Lord, J.: Digital image correlation. Mater. Today **13**, 52–54 (2010)
11. Aly, O., Elias, T.R., Agaibyi, M., Rasheed, W.I., Yassen, N.N., Diab, Y.: Antidiabetic and hepatoprotective activities of bombax ceiba extract in obese rats with metabolic syndrome. Plant Arch. **21**, 748–56 (2021)
12. Holzapfel, G.A., Gasser, T.C., Ogden, R.W.: A new constitutive framework for arterial wall mechanics and a comparative study of material models. J. Elast. Phys. Sci. Solids **61**, 1–48 (2000)
13. Soleimani, M., Deo, R., Hudobivnik, B., Poyanmehr, R., Haverich, A., Wriggers, P.: Mathematical modeling and numerical simulation of arterial dissection based on a novel surgeon view. Biomech. Model. Mechanobiol. **22**, 2097–2116 (2023)
14. Gierig, M., Wriggers, P., Marino, M.: Computational model of damage-induced growth in soft biological tissues considering the mechanobiology of healing. Biomech. Model. Mechanobiol. **20**, 1297–1315 (2021)
15. Rao, R.V., Savsani, V.J., Rao, R.V., Savsani, V.J.: Advanced Optimization Techniques. Springer, Berlin (2012)
16. Ronneberger, O., Fischer, P., Brox, T.: U-net: Convolutional networks for biomedical image segmentation, In: Medical Image Computing and Computer-Assisted Intervention–MICCAI 2015: 18th International Conference, Munich, Germany, October 5-9, 2015, Proceedings, Part III 18, Springer, pp. 234–241 (2015)
17. Bai, J., Jeong, H., Batuwatta-Gamage, C., Xiao, S., Wang, Q., Rathnayaka, C., Alzubaidi, L., Liu, G.-R., Gu, Y.: An introduction to programming physics-informed neural network-based computational solid mechanics. arXiv preprint arXiv:2210.09060 (2022)
18. Goswami, S., Anitescu, C., Chakraborty, S., Rabczuk, T.: Transfer learning enhanced physics informed neural network for phase-field modeling of fracture. Theoret. Appl. Fract. Mech. **106**, 102447 (2020)
19. Linden, L., Klein, D.K., Kalina, K.A., Brummund, J., Weeger, O., Kästner, M.: Neural networks meet hyperelasticity: a guide to enforcing physics. J. Mech. Phys. Solids **179**, 105363 (2023)
20. As'ad, F., Farhat, C.: A mechanics-informed deep learning framework for data-driven nonlinear viscoelasticity. Comput. Methods Appl. Mech. Eng. **417**, 116463 (2023)
21. Aldakheel, F., Haist, M., Lohaus, L., Wriggers, P.: Machine learning for the numerical homogenization of concrete. Bauingenieur **98**, 354–360 (2023)
22. Fuchs, A., Heider, Y., Wang, K., Sun, W., Kaliske, M.: Dnn2: a hyper-parameter reinforcement learning game for self-design of neural network based elasto-plastic constitutive descriptions. Comput. Struct. **249**, 106505 (2021)
23. Zohdi, T.I., Zohdi-Mofid, M.: Rapid machine-learning enabled design and control of precise next-generation cryogenic surgery in dermatology. Comput. Methods Appl. Mech. Eng. **417**, 116220 (2023)
24. Krizhevsky, A., Sutskever, I., Hinton, G. E.: Imagenet classification with deep convolutional neural networks. Adv. Neural Inf. Process. Syst. **25** (2012)
25. Girshick, R., Donahue, J., Darrell, T., Malik, J.: Rich feature hierarchies for accurate object detection and semantic segmentation. In: Proceedings of the IEEE Conference on Computer Vision and Pattern Recognition, pp. 580–587 (2014)
26. Chaaban, M., Heider, Y., Sun, W., Markert, B.: A machine-learning supported multi-scale lbm-tpm model of unsaturated, anisotropic, and deformable porous materials. Int. J. Numer. Anal. Methods Geomech. (2023)
27. LeCun, Y., Boser, B., Denker, J.S., Henderson, D., Howard, R.E., Hubbard, W., Jackel, L.D.: Backpropagation applied to handwritten zip code recognition. Neural Comput. **1**, 541–551 (1989)
28. Aldakheel, F., Soyarslan, C., Palanisamy, H.S., Elsayed, E.S.: Machine learning aided multiscale magnetostatics. Mech. Mater. **184**, 104726 (2023)
29. Eidel, B.: Deep CNNS as universal predictors of elasticity tensors in homogenization. Comput. Methods Appl. Mech. Eng. **403**, 115741 (2023)
30. Aldakheel, F., Elsayed, E.S., Zohdi, T.I., Wriggers, P.: Efficient multiscale modeling of heterogeneous materials using deep neural networks. Comput. Mech. **72**, 1–17 (2023)
31. Stöcker, J.P., Elsayed, E.S., Aldakheel, F., Kaliske, M.: FE-NN: efficient-scale transition for heterogeneous microstructures using neural networks. PAMM **23**, e202300011 (2023)
32. Asgharzadeh, P., Röhrle, O., Willie, B.M., Birkhold, A.I.: Decoding rejuvenating effects of mechanical loading on skeletal aging using in vivo μct imaging and deep learning. Acta Biomater. **106**, 193–207 (2020)
33. Alloisio, M., Gasser, T.C.: Fracture of porcine aorta-part 2: FEM modelling and inverse parameter identification. Acta Biomater. **167**, 158–170 (2023)
34. Yeoh, O.H.: Some forms of the strain energy function for rubber. Rubber Chem. Technol. **66**, 754–771 (1993)
35. Gasser, T., Auer, M., Labruto, F., Swedenborg, J., Roy, J.: Biomechanical rupture risk assessment of abdominal aortic aneurysms. Model complexity versus predictability of finite element simulations. Eur. J. Vasc. Endovasc. Surg. **40**, 176–185 (2010)
36. Barenblatt, G.I.: The mathematical theory of equilibrium of cracks in brittle fracture. Adv. in Appl. Mech. **7**, 55–129 (1962)
37. Dugdale, D.: Yielding of steel sheets containing slits. J. Mech. Phys. Solids **8**, 100–104 (1960)
38. Holzapfel, G.A., Gasser, T., Stadler, M.: A structural model for the viscoelastic behavior of arterial walls: continuum formulation and finite element analysis. EURJM **21**, 441–463 (2002)
39. Oktay, O., Schlemper, J., Folgoc, L. L., Lee, M., Heinrich, M., Misawa, K., Mori, K., McDonagh, S., Hammerla, N. Y., Kainz, B., et al.: Attention u-net: learning where to look for the pancreas. arXiv preprint arXiv:1804.03999 (2018)
40. Alom, M. Z., Hasan, M., Yakopcic, C., Taha, T. M., Asari, V. K.: Recurrent residual convolutional neural network based on u-net (r2u-net) for medical image segmentation. arXiv preprint arXiv:1802.06955 (2018)
41. Long, J., Shelhamer, E., Darrell, T.: Fully convolutional networks for semantic segmentation. In: Proceedings of the IEEE Conference on Computer Vision and Pattern Recognition, pp. 3431–3440 (2015)
42. Gal, Y., Ghahramani, Z.: Dropout as a Bayesian approximation: representing model uncertainty in deep learning. In: International Conference on Machine Learning, PMLR, pp. 1050–1059 (2016)
43. Dechesne, C., Lassalle, P., Lefèvre, S.: Bayesian deep learning with monte Carlo dropout for qualification of semantic segmentation. In: IEEE International Geoscience and Remote Sensing Symposium IGARSS. IEEE, 2021, pp. 2536–2539 (2021)

44. Xu, X., Zhou, F., Liu, B., Bai, X.: Multiple organ localization in CT image using triple-branch fully convolutional networks. IEEE Access **7**, 98083–98093 (2019)
45. Hernández, Q., Badías, A., Chinesta, F., Cueto, E.: Thermodynamics-informed graph neural networks. arXiv preprint arXiv:2203.01874 (2022)
46. Franke, M., Klein, D.K., Weeger, O., Betsch, P.: Advanced discretization techniques for hyperelastic physics-augmented neural networks. Comput. Methods Appl. Mech. Eng. **416**, 116333 (2023)
47. Fuhg, J.N., Bouklas, N.: On physics-informed data-driven isotropic and anisotropic constitutive models through probabilistic machine learning and space-filling sampling. Comput. Methods Appl. Mech. Eng. **394**, 114915 (2022)
48. Weber, P., Wagner, W., Freitag, S.: Physically enhanced training for modeling rate-independent plasticity with feedforward neural networks. Comput. Mech. **72**, 1–31 (2023)
49. Harandi, A., Moeineddin, A., Kaliske, M., Reese, S., Rezaei, S.: Mixed formulation of physics-informed neural networks for thermo-mechanically coupled systems and heterogeneous domains. Int. J. Numer. Meth. Eng. **125**, e7388 (2024)
50. Stender, M., Ohlsen, J., Geisler, H., Chabchoub, A., Hoffmann, N., Schlaefer, A.: U p-net: a generic deep learning-based time stepper for parameterized spatio-temporal dynamics. Comput. Mech. **71**, 1227–1249 (2023)